Colloids and Surfaces A: Physicochemical and Engineering Aspects 704 (2025) 135524

Contents lists available at ScienceDirect

Colloids and Surfaces A: Physicochemical and Engineering Aspects

journal homepage: www.elsevier.com/locate/colsurfa

Enhancement of corrosion, biocompatibility and drug delivery properties of nitinol implants surface by Al-Zn-LDH nanohybrids

Mehrdad Khakbiz [a,*], Milad Chagami [b], Saeed Sheibani [c], Elahe Amiri [b], Seyedsajad Moazzeni [d], Sara Shakibania [f], Yannan Hou [e], Ki-Bum Lee [e]

[a] Department of Chemical and Biochemical Engineering, Rutgers, The State University of New Jersey, Piscataway, NJ, USA
[b] Division of Biomedical Engineering, Faculty of New Sciences and Technologies, University of Tehran, North Kargar Ave, Tehran, Iran
[c] School of Metallurgy and Materials Engineering, College of Engineering, University of Tehran, Tehran, Iran
[d] Department of Biomedical Engineering, Rutgers, The State University of New Jersey, Piscataway, NJ, USA
[e] Department of Chemistry and Chemical Biology Rutgers, The State University of New Jersey, Piscataway, NJ 08854, USA
[f] Department of Physical Chemistry and Technology of Polymers, Silesian University of Technology, Gliwice, Poland

GRAPHICAL ABSTRACT

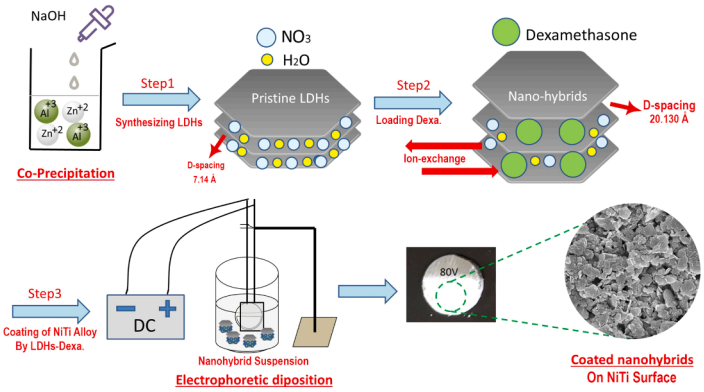

ARTICLE INFO

Keywords:
Nitinol
Surface coating
Layered double hydroxide (LDH)
Drug delivery
Corrosion

ABSTRACT

This study investigates the enhancement of drug delivery and corrosion resistance by incorporating dexamethasone sodium phosphate into aluminum-zinc layered double hydroxide (LDH) coated nickel-titanium alloys. The nickel-titanium samples were fabricated from titanium and nickel powders using spark plasma sintering (SPS) and cold press sintering (CPS), followed by electrophoretic deposition of LDH nanoparticles. This composite construction aims to utilize the biocompatibility and mechanical properties of nickel-titanium, combined with the controlled drug release and corrosion resistance properties of LDH coatings. Structural and microstructural characterizations were performed using X-ray diffraction and scanning electron microscopy. The results indicated that SPS samples exhibited superior microstructural homogeneity and corrosion resistance compared to CPS samples. Dexamethasone sodium phosphate was successfully intercalated into the LDH layers, as evidenced by an increase in layer spacing from 7.14 Å to 20.130 Å. The LDH-coated nickel-titanium with intercalated

* Corresponding author.
E-mail address: Mehrdad.khakbiz@rutgers.edu (M. Khakbiz).

https://doi.org/10.1016/j.colsurfa.2024.135524
Received 25 February 2024; Received in revised form 29 September 2024; Accepted 6 October 2024
Available online 9 October 2024

dexamethasone sodium phosphate demonstrated a 5 % lower drug release rate and significantly improved corrosion resistance compared to uncoated samples. Cell adhesion studies confirmed good biocompatibility between cells and the coated surface. This composite material shows promise for enhanced performance in biomedical applications, particularly in drug delivery and corrosion resistance.

1. Introduction

Equiatomic NiTi alloys, commonly known as Nitinol, possess several desirable properties, such as excellent biocompatibility, shape memory effects, and strength similar to bone tissue [1,2]. These features make Nitinol highly suitable for biomedical applications, such as bone implants, stents, and guiding wires. However, using metal implants like Nitinol for orthopedic or cardiovascular therapy presents several challenges, including post-implantation diseases and biomechanical issues [3,4]. Therefore, surface modification processes are crucial to adapt the implant surface to the surrounding tissues. Modifying the implant surface with biocompatible materials capable of carrying drugs, anti-allergy, anti-clotting, and other therapeutic agents can reduce pain and accelerate patient recovery [5].

Powder metallurgy (PM) is a widely used method for manufacturing Nitinol due to its numerous advantages. These include reduced energy consumption, homogeneous chemical composition in the alloy, fast production, minimized contamination, and the ability to create complex components. Various methods for fabricating bulk Nitinol using PM have been studied, such as cold press sintering (CPS) and spark plasma sintering (SPS), which are more conventional [6–9]. However, research has shown that CPS alloys may contain an oxygen-rich phase, leading to embrittlement of Nitinol during preparation [10,11]. This occurs when Ni, Ti, and O elements combine to form TiO_2 or $Ti_4Ni_2O_x$ ($1<x<0$) oxides. Porosity in PM parts is an important factor that influences biomechanical stiffness, the surface area that comes into contact with tissue, and the corrosion behavior of the implant. Compared to CPS, which usually has an average of 40 % volume porosity, SPS can fabricate denser Nitinol (12 % volume) with higher strength [7].

Recent advancements in surface modification technologies have led to the development of biocompatible coatings for Nitinol implants to address their limitations, such as low corrosion resistance, ion release, low bioactivity, and post-inflammatory effects. Various methods have been proposed for creating these coatings, including plasma spraying [12], sol-gel [13], immersion [14], ionic implantation [15], biomimetic methods [16], electrophoretic deposition (EPD) [17], electrolytic deposition, and electrochemical techniques [18]. Among these, EPD has gained more attention due to its simplicity, ability to control coating thickness and uniformity, low process temperature, cost-effective equipment, suitability for substrates with various shapes and complexities, high purity of deposited products, and no phase changes during the coating processes [19].

In the past decade, Layered Double Hydroxides (LDH) nanoparticles have gained significant attention as bio-molecule and drug carriers due to their unique ability to host anionic species in their interlayer space [20–22]. LDH nanoparticles belong to a class of laminar compounds, compromising brucites-like host layers with positive charges and interchangeable hydrated anions between them. The chemical composition of LDHs is $[M^{2+}_{1-x2}\ M^{3+}_{x}\ (OH)2]^{x+}[A^{m-}]_{x/m}.nH_2O$, where M^{n+} represents metal cations (e.g., Ca^{2+}), M^{3+} indicates trivalent ions (such as Fe^{3+}, Al^{3+}), and A^{m-} comprises interlayer anions (such as SO_4^{2-}, CO_3^{2-}, NO_3^-). Anions and water molecules are present between the plates of the main layers, forming a complex network of hydrogen bonds between the hydroxyl groups of the layer, anions, and water. These anions can be replaced with bio-molecules and drugs [23]. Recently, the anionic capacity of LDH nanoparticles has led to extensive research on their hybridization with anionic molecules. Studies focus on nanoparticles of LDHs, including Mg, Zn, and Al, with anionic molecules such as nucleotide phosphates [24], deoxyribonucleic acid [25], anti-inflammatory oligonucleotides [26], peptides [27], anti-inflammatory drugs [28], and vitamins [29].

Numerous studies have explored the coating of LDHs onto various metal substrates via different techniques. In 1990, Buchheit and his team [30] developed a series of LDH coatings for aluminum and aluminum alloys using in situ growth methods. Lin et al. [31] later prepared Mg-Al LDH coatings on Al-rich Mg alloys in carbonic acid solutions. More modified procedures using in situ growth strategies have been developed, including hydrothermal treatment [32,33], urea hydrolysis [34], steam coating [35], and more. However, the in situ methods restrict the types of cations used in LDHs and they are typically time-consuming, requiring high temperatures [36].

In 2010, Wang et al. [37] first reported a simple co-precipitation method combined with hydrothermal treatment to prepare a Mg-Al LDH coating on Mg alloy. The LDH coating was found to be compact over the alloy surface. However, the coating had the drawback of forming large aggregates, resulting in a heterogeneous coating. In 2013, Syu and coworkers [38] fabricated a Li-Al-CO_3 LDH coating on Mg alloys using electrochemical deposition. This method was quickly developed, showing advantages of high efficiency and applicability to complex surface geometries but faced limitations due to its complex operation and high cost. EPD, on the other hand, is a simple and effective technique for fabricating uniform thick films under ambient pressure and temperature and has shown promising results in LDH coating. He et al. [39] reported the fabrication of orientated Mg/Al-NO_3-LDH films on an aluminum substrate using the EPD technique. Matsuda et al. [40] developed an EPD-based method for depositing anionic hydrated titanate nanosheets and Mg-Al LDH nanosheets on an ITO-coated glass substrate. Vajedi et al. [41] fabricated a highly sensitive electrochemical DNA biosensor by electrophoretically depositing a Zn/Al LDH-modified cobalt ferrite-graphene oxide nanocomposite on a fluorine tin oxide substrate. The results indicated that nanocomposites had active reaction sites and good electrochemical activity, resulting in a faster and more efficient transfer of electrons on the electrode's surface. Li et al. [42] proposed Ni/Al LDH-modified Ti as a nonenzymatic glucose sensor. The proper adhesion of Ni-Al LDH nanosheet to the Ti substrate made this structure highly stable in electrochemical measurements. Applied voltages and deposition time can be controlled during the density of the deposited layer, crystallinity, and morphology during the EPD process [43,44]. A high EPD voltage can result in a more homogenous and thicker coating, with improved corrosion resistance, but may decrease mechanical and nanoindentation properties [45]. Maleki-Ghaleh et al. [46] used the EPD method to coat NiTi alloy with natural hydroxyapatite, enhancing corrosion resistance compared to uncoated samples. The coating was uniform and dense when samples were coated at 60 V, as opposed to 40 V or 80 V. However, there is currently no study on using the EPD technique to coat LDH nanoparticles on NiTi alloy and intercalate drugs into interlayer spaces of brucite-like platelets.

In this study, NiTi alloys were produced using both CPS and SPS techniques. Physical and mechanical characterization revealed that CPS samples were unsuitable for the deposition process and subsequent drug loading. Therefore, using the EPD technique, SPS samples were chosen for the deposition of Al-Zn-LDH nanoparticles. Dexamethasone (DEXA) was then intercalated into the gaps between the layers of the LDHs, forming a hybrid LDH-DEXA on the Nitinol substrate. UV-Visible and polarization Potentiodynamic Scan (PDS) tests were performed on coated and uncoated samples to investigate drug release over time and corrosion behavior, respectively.

2. Experimental procedure

2.1. Preparation of samples

Elemental powders of nickel (50 % wt.) and titanium (50 % wt.), both with a purity greater than 99 % (Merck®), were mixed for 1 h using a jar mill device to create a 20 g batch of cylindrical powder with a diameter of 20 mm, rotating at 100 rev/min. The particle sizes for Ni and Ti powders were −45 μm and −10 μm, respectively. This mixture was used for pressing and sintering processes. For the CPS process, 3 g of the powder blend were pressed into 10 mm × 10 mm cylinders under a pressure of 1000 MPa. To prevent oxidation of the Ti particles during the sintering process, the green compact samples were vacuumed in a glass compartment. The density of the samples before sintering was calculated from the volume and weight of the compact. Samples were then sintered in a horizontal laboratory furnace at 900 ℃ for 120 min with a heating rate of 50 ℃/min under an argon atmosphere. For the SPS method, 10 g of mixed powder was poured into a graphite die with a diameter of 30 mm. SPS was performed at 900℃ for 10 min with a heating rate of 50 ℃/min under a pressure of 7 MPa in a vacuum atmosphere condition. The sample was cooled in the furnace at a rate of 200 ℃/min for 15 min. The final samples were cut to obtain Nitinol disks with diameters of 10 or 15 mm and a thickness of 0.2 mm.

Following Kamyar et al.'s method [47] and using the co-precipitation, carbonated Al-Zn-LDH nanoparticles were prepared. $Zn(NO_3)_2$ and $Al(NO_3)_3$ (Merck®) were weighted with a Zn/Al molar ratio of 2.1 and dissolved in 100 ml of deionized water. The two solutions were added dropwise to a 1 M Na_2CO_3 solution. Subsequently, a 1 M NaOH solution was added dropwise to deionized water to adjust the pH to 8, and the product was aged on a magnet stirrer (Alfa D-500, Iran) for 24 h at 40 °C. All steps were carried out under a nitrogen atmosphere. After forming a white sediment, the solution was centrifuged at 500 RPM at ambient temperature for 5 min. The resulting powder was washed three times and dried for 18 h. To intercalate Dexamethasone phosphate within the LDH layers, two different amounts of Dexamethasone phosphate (1 g and 0.5 g) were dispersed in 50 ml deionized water by ultrasonication. Then, 1 g of pristine LDH was added to the mixture, and a 1 M NaOH solution was added dropwise to keep the pH at 7. The suspension was stirred for 1 h and then aged at 40°C for 18 h. The remaining steps were similar to the fabrication of LDH [47].

To prepare the suspension liquid, 1 g of Al-Zn-LDH powder was weighed and mixed with 25 ml of ethanol using a magnetic stirrer for 2 h. Ultrasonic dispersers were used to ensure homogeneity and stability of the solid particles for 30 min at each step. Before each deposition stage, the substrate surfaces were ground up to 800 grit, rinsed in acetone and alcohol, and placed in an ultrasonic bath for 30 min. They were then washed with distilled water and dried with a hairdryer. Electrophoretic cells were prepared using a 50 ml beaker equipped with a holder to fix the electrode positions. A steel plate (10 × 20 mm^2) was used as the anode, and a 15 mm disk-shaped Nitinol was used as the cathode. The space between electrodes was about 10 mm, adjusted with special clips. A DC power supply was used to apply fixed potentials of 30, 50, 40, 60, and 80 volts for 2 min. After deposition, the samples were dried in a desiccator for 24 h.

2.2. Characterization

X-ray diffraction (XRD) analysis (Philips PW1730, Netherlands, with a Cu-K_α anode) was conducted to identify the metallic or oxide phases are present on the surface of the as-synthesized bare alloys. XRD was also used to confirm the presence of characteristic crystalline planes in the LDHs and to calculate the spacing between the two-dimensional (2D) layers (d_s) using Bragg's equation. The lattice parameters (A and C) were measured by the distances between the main crystallographic planes [30].

Field emission scanning electron microscopy (FESEM) and scanning electron microscopy (SEM) (TESCAN-MIRA, Czech Republic) were used to analyze the shape of the powder used in the synthesis of the samples, the microstructure of the SPS and CPS components, and the formation of the LDH 2D layer structures, as well as the coating on the Nitinol substrates. Energy dispersive spectroscopy (EDS) was used to determine the elemental composition of the samples. Before the deposition processes, Fourier-transform infrared (FT-IR) spectroscopy was used to assess the formation of LDH structure during the co-precipitation process, to examine the intercalation of the drug between the hydroxide layers, and to detect the presence or absence of nitrate anions in LDHs after drug loading. The IR beam was directed at the powder samples using a WQF 510-FT-IR spectrometer in the wavelength range of 400–4000 cm^{-1}.

2.3. Mechanical evaluations

Mechanical evaluations were conducted on the samples using shear stress and hardness tests. The shear stress test was performed at room temperature using a universal testing machine (STM20, Santam, Tehran, Iran) at a crosshead speed of 0.5 mm/min. Each sample measured 10 mm in length, 2 mm in width, and 1 mm in thickness. Three samples from each group (uncoated CPS, unmilled SPS, and ball-milled SPS) were analyzed to ensure statistical significance.

For the hardness test, a HVS-5 digital Vickers hardness tester was employed with a 5Kgf load and a dwell time of 10 seconds. The same sample dimensions as used in the shear stress test (10 mm length, 2 mm width, and 1 mm thickness) were maintained. Three measurements were taken from each sample to determine the average hardness value.

2.4. Contact angle measurements

To investigate the effect of LDH nanoparticle deposition on the wettability and hydrophilicity of Nitinol substrates, contact angle (CA) values were measured for bare Nitinol. Samples were coated using the sessile drop technique, where a device with a camera captured a highly focused image, and a syringe was used to drop the liquid droplet onto the specimen surfaces. Before testing, the uncoated specimens were mechanically polished with silicon carbide sheets (grit size 1000) and ultrasonically cleaned in acetone. A 1 μl water droplet was applied to the disk-shaped sample.

2.5. Corrosion study

To investigate the corrosion behavior of uncoated and coated Nitinol specimens in a physiological environment, a potentiostat/galvanostat ZAHNER model 96317 Kronach was used to apply a potential rate of 1 mV/s. An electrochemical cell was set up with an auxiliary platinum electrode as the test electrode and a silver/silver-chloride reference electrode. A conventional physiological solution of Phosphate-buffered saline (PBS) was used at pH 7.34 and at 37°C served as the corrosion electrolyte. Tafel linear extrapolation polarization curves and Stern-Geary (ASTM G-59) were used to calculate potential and corrosion density [48].

2.6. Release investigation of dexamethasone

The release test was conducted by the NANODROP 2000 C device (Biomedical Science Laboratory, Faculty of New Science and Technology, University of Tehran, Iran) to evaluate the release rate of DEXA from LDHs and the coating on the Nitinol substrate. Samples were diluted with PBS and poured in a special flask. At specified intervals, 2 ml of the solution was removed and replaced with fresh PBS. Data obtained at different intervals were arranged for various samples. To determine the wavelength with the highest UV absorption for DEXA, 10 mg/L DEXA solution was used in PBS at pH=7.34 and 37 ℃. The maximum Ultraviolet (UV) absorbance for the solution was 242 nm, which was used to calculate the release of the drug from LDHs. A DEXA

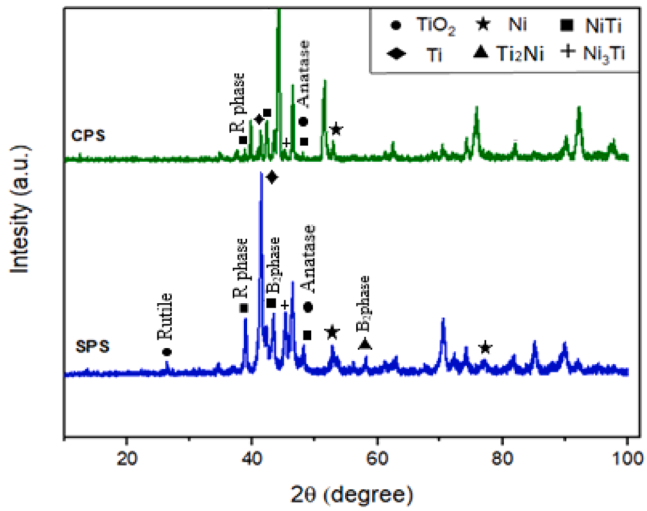

Fig. 1. XRD patterns for the bare SPS and CPS Specimens.

base solution was prepared in PBS to draw the calibration curve, and UV absorbance was measured using UV light spectroscopy.

2.7. Release kinetics study

Estimating release kinetics is complex. This study employed three simplified kinetic models: pseudo-first-order, pseudo-second-order, and parabolic diffusion, to describe the release rate of DEXA from LDHs and coating hybrids, and the best-fitted data were analyzed. Drug dissolution and release involve surface disintegration and diffusion. The constant coefficient k in kinetic equations represents the rate of surface reaction and particle diffusion.

The Lagergren equation, or quasi first-order model, is widely used to describe release rate [49,50].

The linear form is:

$$\log(Q_e - Q_t) = \log Q_e - k_1 t / 2.3 \quad (1)$$

In this equation, Q_e and Q_t are the total release amount and the release amount at each time (t), respectively. k_1 (min^{-1}) represents the rate constant of the quasi-first-order. Another commonly used equation for estimating the kinetics of the release process is the quasi-second-order, which can predict long-term release behavior from experimental data. This relation is expressed as [48]:

$$t/Q_t = 1/k_2 Q_e^2 + t/Q_e \quad (2)$$

Here, Qe and Qt are the same as before, and k_2 is the rate constant of quasi-second-order. The parabolic diffusion kinetic model is frequently employed to characterize the release kinetics of DEXA from clay nanohybrids, where diffusion within particles governs the process. The linearized representation of this model is depicted as [51], where X_t and k_3 denote the release percentage and kinetic constant, respectively.

$$(1\text{-}X_t)/t = k_3 t^{-0.5} + a \quad (3)$$

2.8. In-vitro cell adhesion evaluation

The NIH 3T3 mouse embryonic fibroblast cell line (NCBI code: C156, Pasteur Institute, Tehran, Iran) was used to investigate the cell adhesion and proliferation capabilities of the coated Nitinol samples. Cells were cultured in Dulbecco's Modified Eagle Medium (DMEM) supplemented with 10 % Fetal Bovine Serum (FBS) in plastic flasks and incubated at 37 ℃ in a 5 % CO_2 atmosphere. The coated samples were exposed to the medium for 24 h and then incubated under the same conditions. SEM images were taken to assess the morphology and apparent proliferation of the cells on the surface.

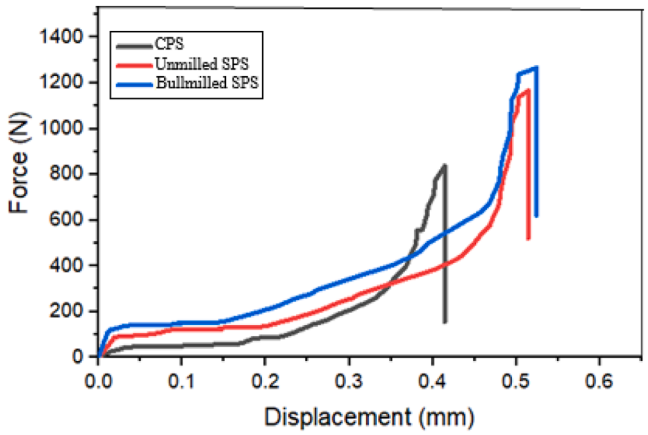

Fig. 2. Mechanical properties of CPS, element SPS and ball milled samples.

3. Results and discussion

3.1. Phase analysis of consolidated nitinols

Fig. 1 illustrates the XRD patterns for both CPS and SPS samples. Notably, CPS samples exhibited a higher presence of oxide phases compared to SPS samples, likely due to exposure to oxygen in a less vacuum-sealed glass compartment. This oxidation phenomenon can be attributed to the presence of titanium in the alloy, which at elevated temperatures increases the Gibbs free energy (ΔG), rendering the alloy thermodynamically unstable during sintering processes. Both CPS and SPS samples exhibit phases including Ni,Ti, TiO_2, Ni_3Ti, Ti_2Ni, and NiTi after sintering durations of 120 and 30 minutes, respectively. Peaks at 26.18° correspond to the TiO_2 Rutile phase (JCPDS Card No. 21–1276), and the peak at 48.2° corresponds to the TiO_2 Anatase phase (JCPDS Card No. 21–1272). The peak at 38.8° represents the NiTi R phase (JCPDS Card No. 35–0787), and at 43.4° it corresponds to the B_2 phase of NiTi (JCPDS Card No. 35–0788). Peaks at 52.6° and 76.8° are associated with Ni (JCPDS Card No. 04–0850), while the peak at 41.4° corresponds to the Ti alpha phase (JCPDS Card No. 44–1294). The peak at 45.2° is related to Ni_3Ti (JCPDS Card No. 35–0789), and the peak at 58.2 ° is associated with the B_2 phase of Ti_2Ni (JCPDS Card No. 65–0621) [52,53]. Incomplete conversion reactions were observed for the formation of NiTi, likely due to heterogeneous regions of nickel and titanium in the samples before sintering, leading to localized high concentrations of these elements and subsequent formation of Ni3Ti and Ti2Ni compounds [52,54]. Consequently, we used SPS samples for coating since the CPS specimen lacked electrical current during the deposition process. The conductivity of the substrate is a determining parameter in the deposition process, as deposition occurs only on conducting surfaces [55]. EPD involves the deposition of charged powder particles dispersed in a liquid medium onto a substrate with opposite charge in a DC electric field [56]. Therefore, a conductive substrate is required to establish the necessary electrical path [57].

Table 1
Mechanical properties of samples.

Samples	F_{max} (N)	T_{max} (Mpa)	σ_u(Mpa)	Hardness (Hv_{10})
CPS	822.43	78.26	124.43	58
Unmilled SPS	1183.3	109.64	174.32	674
Ballmilled SPS	1242.8	113.60	180.624	678.13

Table 2
Physical properties of samples.

Samples	Porosity (%)	Density(g/Cm^3)
CPS	42	5.23
Unmilled SPS	13.2	5.84
Ballmilled SPS	12.34	6.092

3.2. Mechanical properties of consolidated nitinols

The results of the shear stress test performed on three samples: uncoated CPS, unmilled SPS, and ball-milled SPS, are presented in Fig. 2 and Table 1. These results indicate that CPS samples have significantly lower final shear and tensile strength due to their higher porosity and the presence of brittle oxide phases. The effect of mechanical alloying on SPS samples is also evident, with ball-milled SPS samples showing higher strength. Mechanical alloying enhances the mechanical bonding

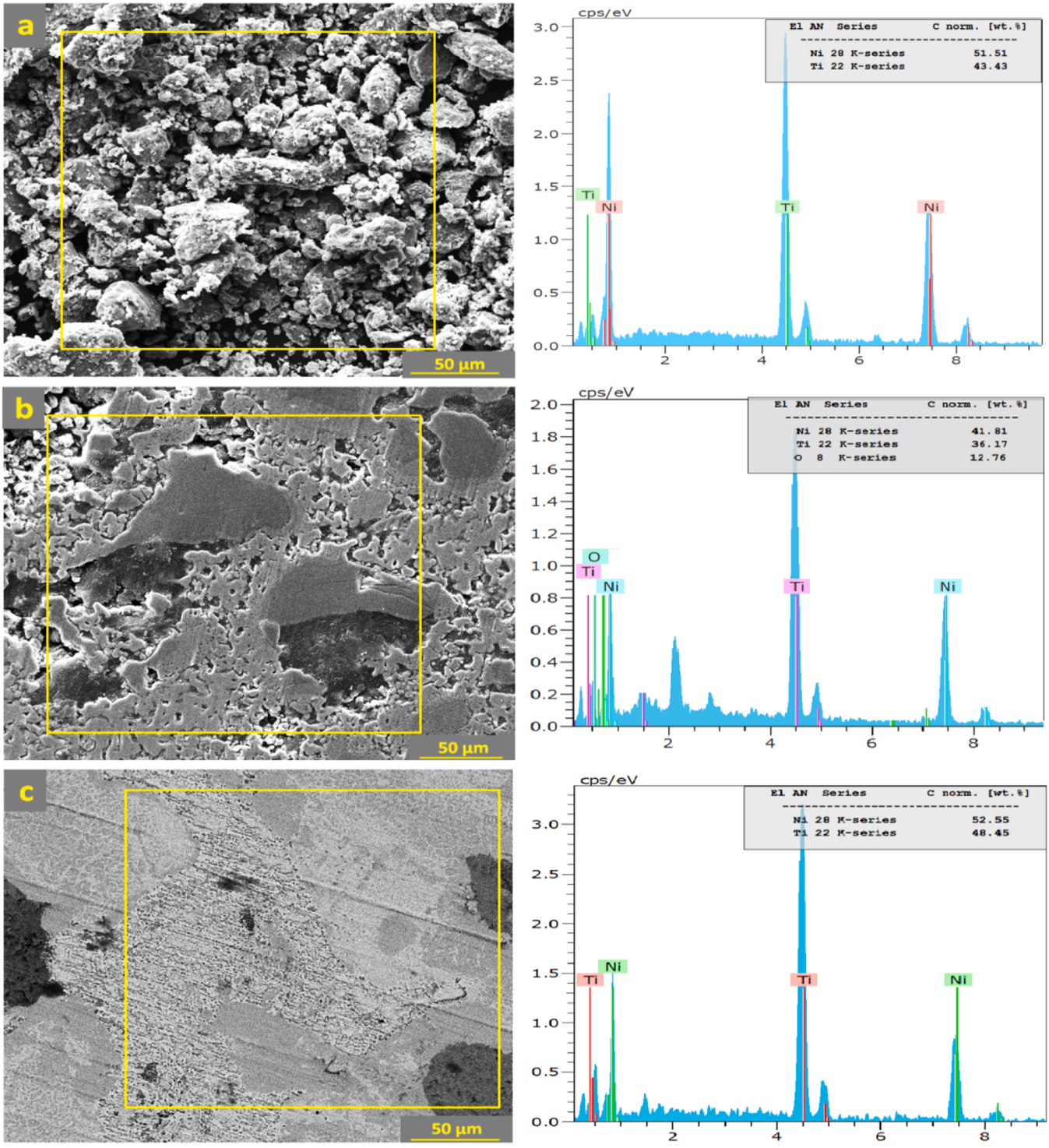

Fig. 3. SEM images and EDX analysis of (a) powder mixture of elemental Ti and Ni, (b) CPS specimen after 120 min sintering at 900 ℃, and (c) SPS sample after 120 min sintering at 900 ℃.

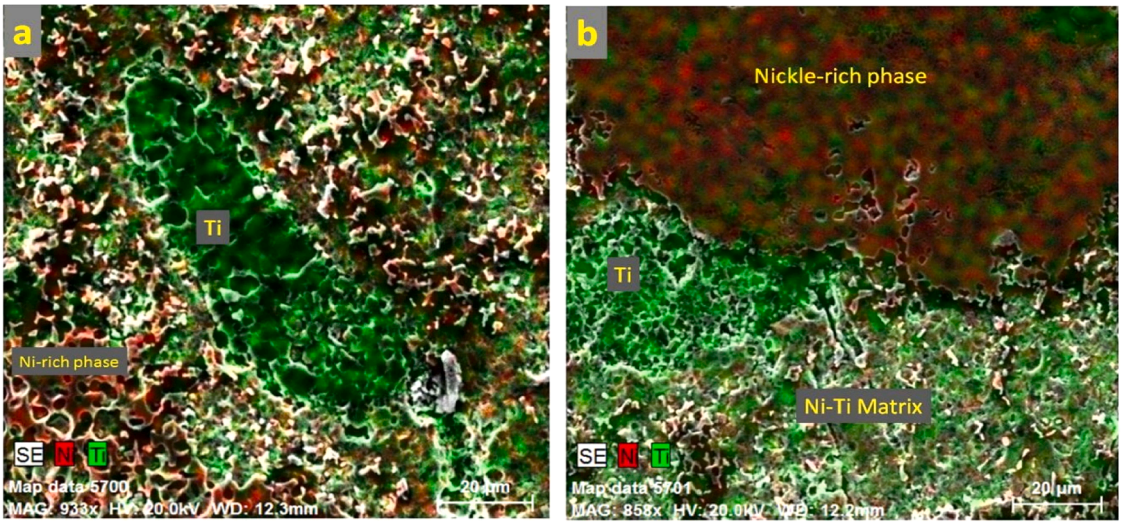

Fig. 4. Secondary electron SEM elemental map of a chemically etched SPS Nitinol sample.

of powders, and increasing the temperature to near the melting point reduces penetration time, improving the alloying opportunity for the particles. Consequently, the formation of the NiTi matrix phase is associated with greater flexibility and robustness.

Table 2 presents the results of the hardness measurements, average porosity percentage, and densitometry for the aforementioned samples. As expected, CPS samples have lower density compared to SPS samples due to 42 % porosity and the presence of oxide compounds in the alloy. The impact of mechanical alloying on the density of SPS samples is also apparent, with ball-milled samples having higher density due to reduced porosity. Notably, the hardness test results showed that Ti_2Ni and Ni_3Ti intermetallic compounds are significantly harder compared to the NiTi matrix phase, and are more abundant in SPS samples. Conversely, CPS samples exhibit less resistance to indentation under applied pressure, likely due to the numerous voids between the material phases on the surface, resulting in lower hardness values.

3.3. Surface and particle morphologies and multifractal analysis

SEM images in Fig. 3**a** clearly illustrate the geometric shape and distribution of the nickel and titanium powder mixture, with fine Ni particles distributed among the coarse, irregularly shaped Ti particles. There is no evidence of mechanical alloying occurring between the particles. Fig. 3**b-c** display SEM images of components produced by the CPS and SPS methods, respectively. The higher porosity of the CPS samples compared to SPS samples is evident. Additionally, the microstructure homogeneity and distribution of metallic compounds within the NiTi matrix suggest that the SPS samples exhibit better conditions, indicative of superior alloying [58]. Surface analysis of Nickel, Titanium, and Oxygen reveals the elemental composition on the surface. CPS samples show a significant percentage of surface oxygen, which has interfered with the alloying process. Titanium's high reactivity with oxygen and the increased porosity of CPS samples render them more prone to oxidation. Furthermore, the furnace atmosphere was not adequately controlled, exacerbating oxidation, which is a common issue in studies involving Nitinol and other metals [11,59–61]. The successful alloying in SPS samples is demonstrated by the nearly equal percentages of nickel and titanium on the surface, whereas the oxide phases in CPS samples made them unsuitable for the EPD process. To further investigate the intermetallic compounds on the SPS sample surfaces, elemental mapping and secondary SEM images were taken from the etched surfaces of two areas of an SPS-Ni-Ti sample (see Fig. 4). The images show that the Ni-Ti matrix was more extensively corroded during the etching process. Fig. 4**a** highlights an area with a single-phase Ti, while Fig. 4**b** represents a nickel-rich phase, such as Ni_3Ti.

Fig. 5**a-c** depict the SEM images of LDHs, LDH-DEXA (1:0.5), and LDH-DEXA (1:1) particles. The LDH nanohybrids exhibit a plate-like shape with a polyhedral morphology. As the DEXA content increases, there is a slight increase in particle thickness, and the sharpness of the particle edges reduces [62]. Furthermore, drug molecule incorporation inside the structure is observed to increase particle agglomeration. Fig. 5**d-e** present particle size distribution curves of pure LDH and LDH loaded with two different ratios of DEXA. Pure LDH exhibits finer particles (D_{mean}=503 nm) with a narrower distribution, while LDH-DEXA shows coarser particles (D_{mean}=920 nm, and D_{mean}=1180 nm) with broader distribution curves.

Fractal theory is employed to study nonlinear and irregular characteristics of particle shapes. As shown in Fig. 5, most particles exhibit nonlinear and irregular shapes. Previous studies have suggested that particle complexity can be characterized by a fractal distribution [46, 62], which was applied in this study using the ImageJ toolbox software. The results in Fig. 5 f. show that theoretically, the fractal dimension of particles range from 1.0 to 2.0, where 1.0 represents complete homogeneity, and 2.0 represents the ideal heterogeneous state of particles. Fig. 5**f** indicates that LDH particles have the highest fractal dimension (Ds= 1.81) and the narrowest multifractal spectrum. In contrast, the intercalation of DEXA with ratio a of 1:0.5 and 1:1 results in lower fractal dimensions (1.76, 1.73).

Fig. 6 displays low-magnified SEM images of Nitinol samples coated with LDHs deposited at 30, 40, 50, 60, and 80 V for 120 s. The image reveals that the sample coated at 50 V exhibits a relatively uniform coating compared to the other voltages. However, Fig. 6**b** shows a darker area where LDHs are not successfully deposited, indicating that 30 V was insufficient to drive the LDH particles to the Nitinol surface within 2 minutes. Moreover, at 40 V, the coating attachment was inadequate, resulting in cracks in the coating during drying. The density of the coating depends on factors such as suspension stability and physical conditions during deposition, such as applied voltage. Enhanced suspension stability reduces particle agglomeration and sedimentation, resulting in a more uniform coating [63]. The applied voltage determines the force applied to suspension particles. Higher voltage increases the electrophoretic force, causing more particles to collide with the Nitinol surface and leading to a denser coating. However, excessive voltage can also increase porosity due to hydrogen evolution at the cathode [46], which may result in coating cracks after drying **(**Fig. 6**e-f)**. Therefore, selecting an optimal voltage range to balance coating density and porosity is crucial, and 50 V was chosen for this study.

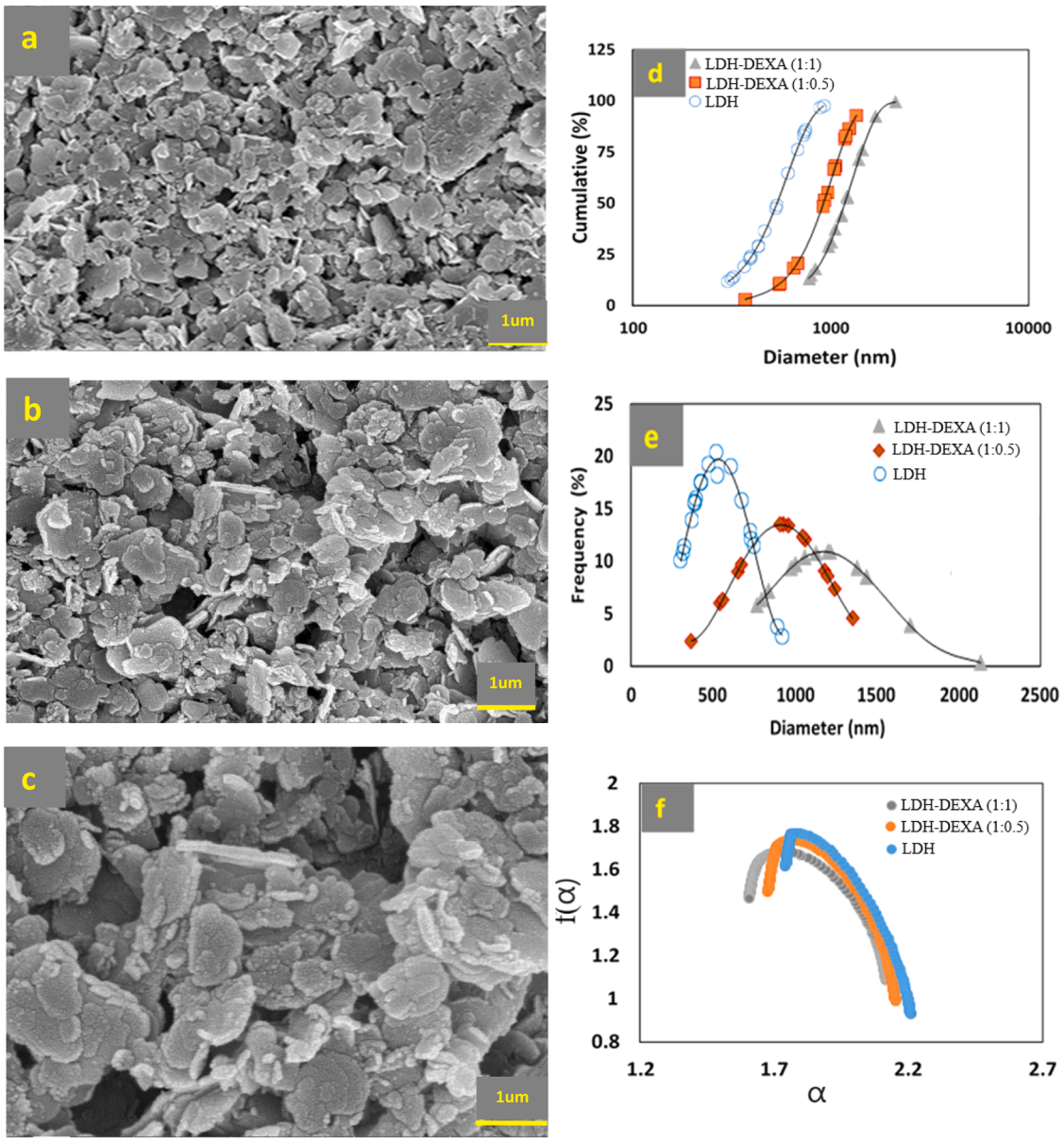

Fig. 5. (a- c) SEM images of LDHs and LDH-Dexamethasone nanohybrids, (d,e) Normal and cumulative particle size distribution curves of nanohybrids, (f) Multifractal spectrums of the three types of nanoparticles.

Fig. 7 illustrates the morphology of LDHs nanoparticles coated on the Nitinol surface at 50 V and 80 V, along with a side view to examine the effect of voltage on thickness. In Fig. 7**a,** hexagonal-like platelets of LDH nanoparticles are observed, coating the Nitinol surface in an almost 2D manner. The micro-porous structure visible in the coating is attributed to hydrogen bubbles on the surface that burst during deposition. The nanoplates are not fully stacked, leading to the formation of nano-ducts in the thickness of the coating. Increasing the voltage from 50 V to 80 V results in an increase in coating thickness from 19.52 μm to 29.72 μm, respectively, due to higher particle deposition [39,46]. The histogram charts in Fig. 7**e** depict the size distribution of surface pores, revealing significantly larger pore sizes in coatings deposited at 80 V compared to 50 V, with average sizes of 10.17 nm and 4.23 nm, respectively. This difference may be attributed to surface cracks and increased thickness at 80 V. Additionally, surface microhardness measurements at 30 V, 40 V, 50 V, 60 V, and 80 V yielded values of 200 HV, 212 HV, 245 HV, 278 HV, and 302 HV, respectively, reflecting increased hardness with thicker coatings resulting from higher voltage application.

3.3.1. *Surface topography*

Surface topography is a critical parameter for evaluating coating properties. Mountains®9 software was used to analyze surface roughness characteristics of both coated and uncoated. A 3D image of the sample surfaces is shown in Fig. 8. Subsequently, roughness and waviness parameters were determined using the software, as depicted in Fig. 9, with corresponding values presented in Table 3. It is evident that roughness and waviness parameters generally exhibit higher values for coated samples, with uncoated ball-milled SPS samples showing the lowest values. Among the coated samples, the sample coated at 50 V exhibits the minimum value.

3.4. *Evaluation of intercalation*

XRD patterns of LDHs, NITi-coated LDH, and NITi-coated LDH loaded with DEXA are presented in Fig. 10. The green line represents the XRD pattern of pristine LDHs powder, characterized by three distinct low angle, symmetric, crystalline, and sharp peaks, corresponding to the basal reflection of LDHs layers, as reported in previous studies [39,64].

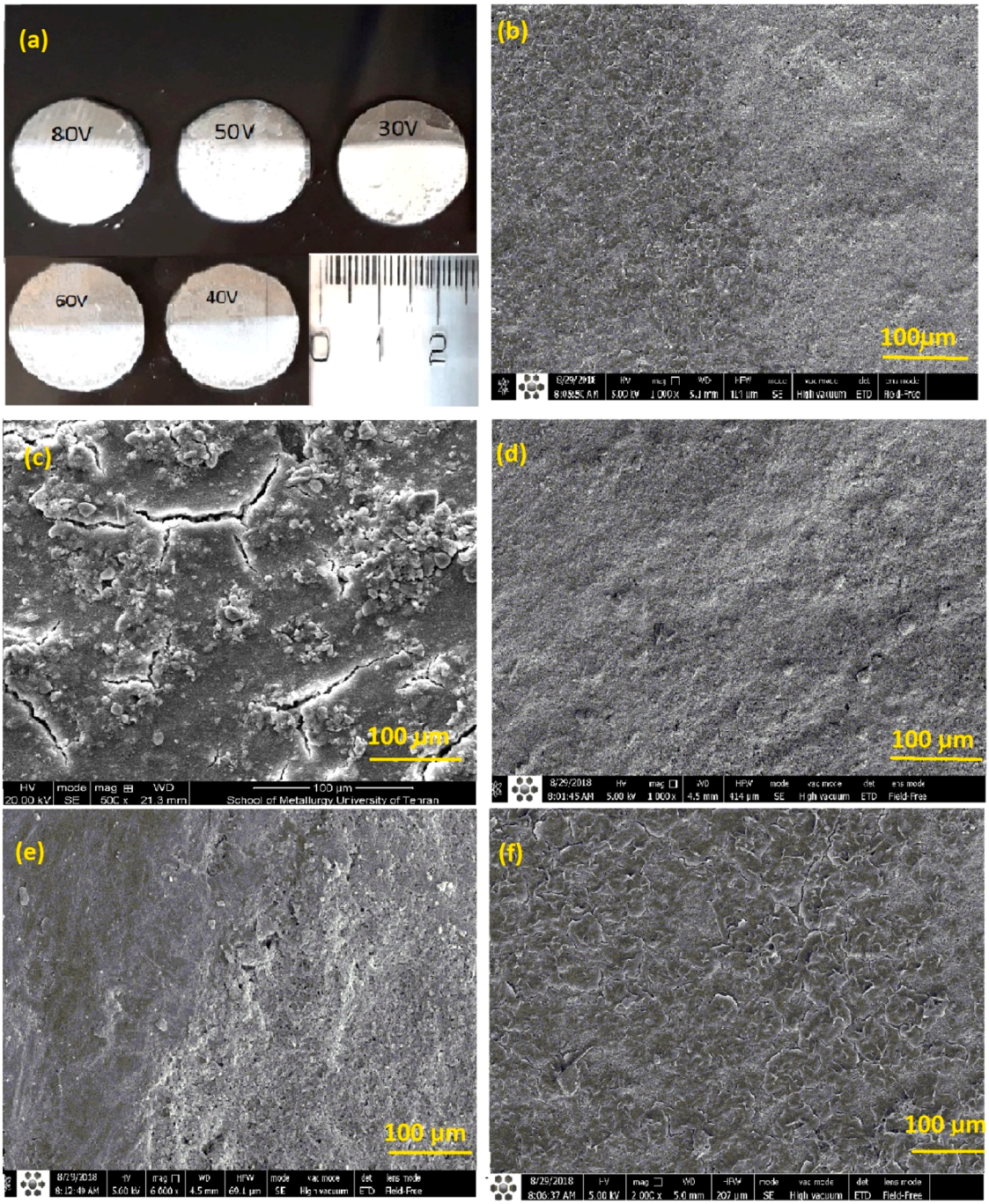

Fig. 6. (a) Different samples and SEM images of Al-Zn-LDH EPD coating on Nitinol substrates at (b) 30 V, (C) 40 V, (d) 50 V, (e) 60 V, and (f) 80 V at constant deposition time of 2 min.

The 110 peak signifies the structural integrity resembling brucite-like layers. Coated NiTi specimens with pristine LDHs do not exhibit non-basal reflections such as (015) and (110). Additionally, the intensity of NiTi peaks is lower compared to the uncoated sample. The addition of DEXA reduces the intensity of main peaks, causing them to shift to lower angles and broaden (Fig. 10**a)**, indicating disruption of crystalline order due to the incorporation of the hydrophobic drug. Table 4 presents measurements of the d003 and lattice parameters for various Al-Zn-LDH peaks and hybrids after drug intercalation. The values were derived from (003) and (110) reflections, where A=2d110 and C=3d003. The d003 value for pristine LDHs is approximately 7.1 Å, consistent with literature values [64]. Upon DEXA intercalation, the d003 spacing significantly increases with drug content, suggesting drug molecules are effectively trapped between LDH layers [65].

FT-IR spectra of NO_3^- type LDHs exhibit a broad peak around 3450 cm^{-1} (Fig. 10**b**), attributed to OH group vibrations, resembling brucite-like structures with interlayer water molecules. The peak at 430 cm^{-1} signifies the HO-Al-Zn-OH composition, and the peak at 960 cm^{-1} indicates Al-OH bond deformation. Peaks at 553 cm^{-1} and 766 cm^{-1} indicate Al-OH transition modes, confirming the layered LDH structure. The peak at 1640 cm^{-1} corresponds to the bending vibration of interlayer water, while peaks at 625 cm^{-1} and 1375 cm^{-1} indicate the presence of nitrate (NO_3^-) anions [66–68]. Peaks at 2370 cm^{-1}, 1500 cm^{-1}, and 1718 cm^{-1} are characteristic of DEXA, observed in both LDH nanohybrid samples [64]. The FTIR spectrum of LDH-DEXA hybrids reveals reduced peaks for NO_3^-, suggesting incomplete

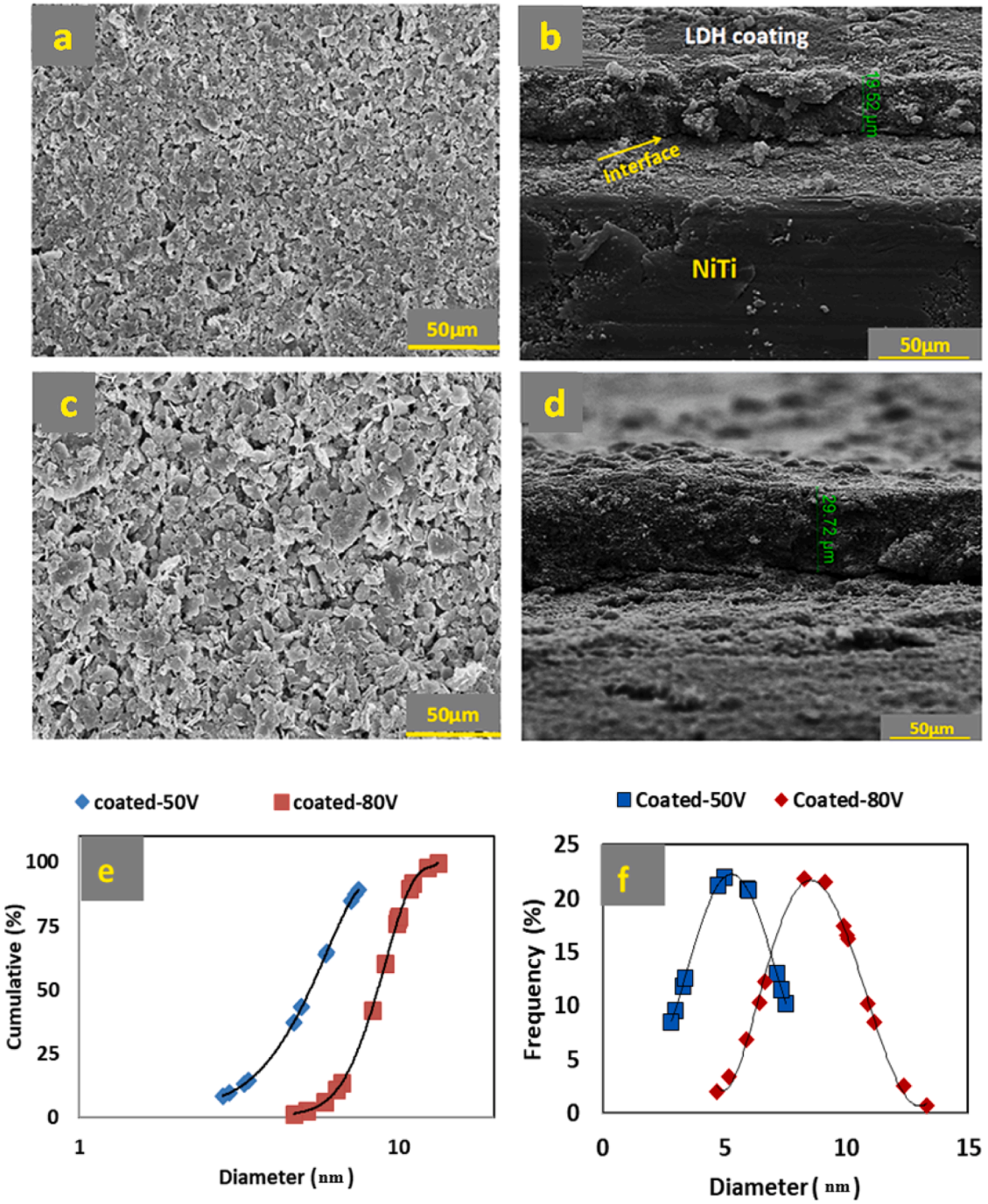

Fig. 7. (a,c) FESEM images showing the LDHs-DEXA coating on Nitinol surfaces, (b,d) Cross-section of the coated surface (with a thickness of 19.22 µm), (e) Histogram charts displaying the size distribution of surface pores for coated samples at 50 V and 80 V, and (f) Cumulative graph of measured pore diameters of the coated surfaces.

replacement by the drug. Nonetheless, the drug's presence is evident and increases with higher DEXA content [47]. A schematic depiction of the intercalation process is presented in Fig. 11, illustrating changes in basal and gallery spacing. No significant peak shifts were observed before and after drug intercalation, with characteristic wave numbers similar to dexamethasone phosphate and the pure drug [64].

3.5. Drug release and kinetic

Fig. 12 **a-b** presents the calibration plot for DEXA at 242 nm and the release profiles of DEXA sodium phosphate from various samples. Three different specimens were tested: Al-Zn-LDH hybrids with DEXA at weight ratios of 1:1 and 1:0.5, and coated Nitinol samples. As shown in Fig. 12**b**, DEXA in uncoated LDHs exhibits a faster release rate, whereas the drug loaded into LDH coatings shows a more controlled release over time, likely due to its incorporation within and between LDH layers [62, 63]. Previous studies have indicated an initial burst release of DEXA within the first 120 minutes, with approximately 85 %, 80 %, and 70 % of the drug released, followed by a slower release in subsequent time intervals [64]. This behavior is influenced by the drug's high hydrophilicity, weak electrostatic interactions between DEXA molecules and LDH surfaces [58,69], and the formation of secondary layers on LDH

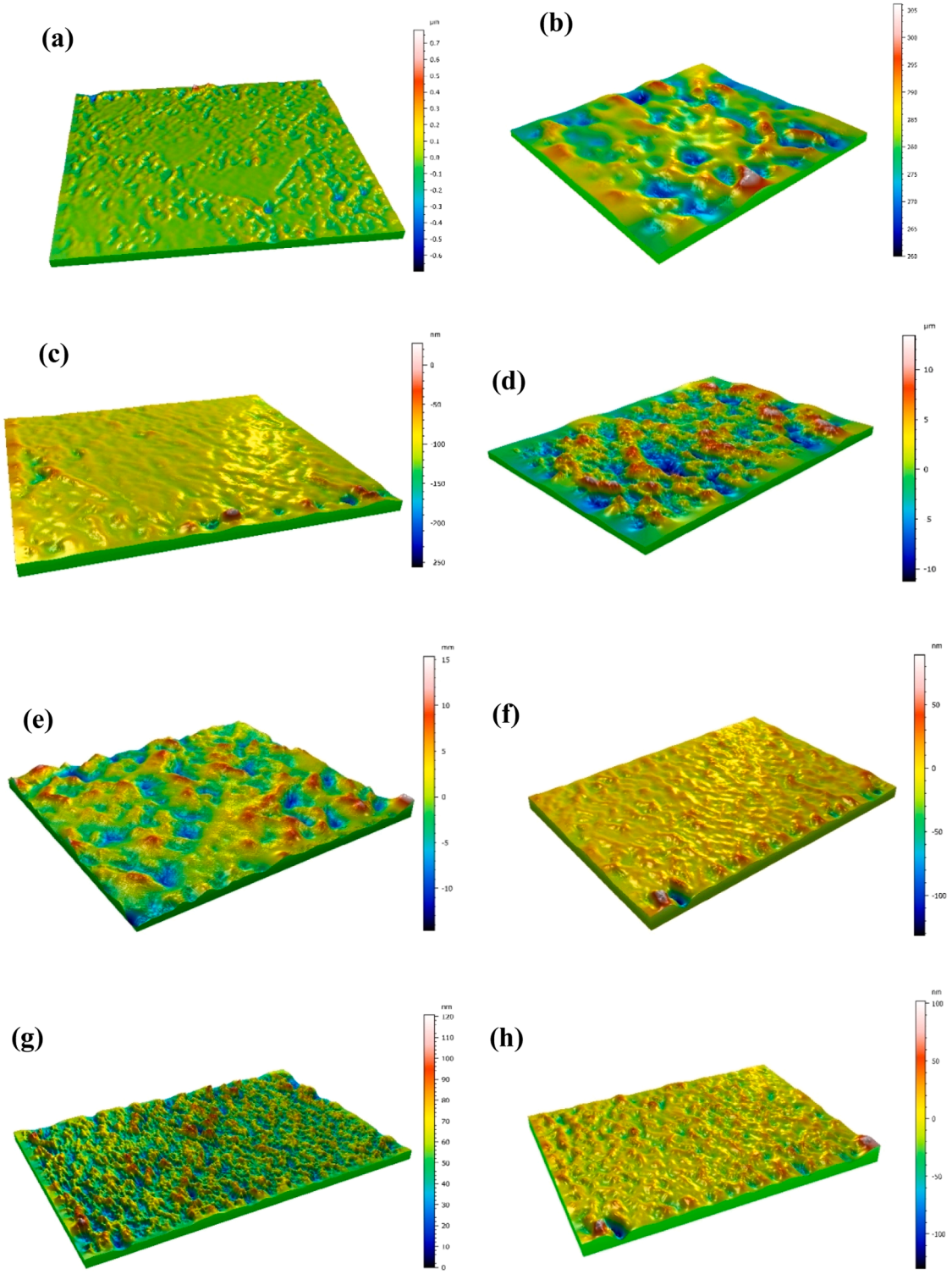

Fig. 8. 3D surface images of different samples, including (a) CPS, (b) SPS, (c) Ball milled SPS, and coated samples at different voltages: (d) 30 V, (e) 40 V, (f) 50 V, (g) 60 V, and (h) 80 V. The images were obtained using Mountains®9 software.

surfaces [64]. According to literature, a two-step release approach enhances therapeutic efficacy: the initial rapid release provides a therapeutic dose, while sustained release maintains the therapeutic levels over an extended period [69]. Furthermore, simultaneous leaking of metal ions during dissolution and ion exchange processes results in competition between phosphate ions in the solution and DEXA phosphate anions in LDH interlayer spaces [64]. Experimental data were fitted to various kinetic models to identify the most suitable model for describing release profiles, with correlation coefficients (R^2) calculated accordingly. Table 5 summarizes the R^2 values for the three equations and different samples. As depicted in Fig. 12**c**, the first-order model shows linear fitting only up to approximately 4 hours, with lower R^2 values compared to the other models (see Table 5), indicating its unsuitability for describing the complete release kinetics of DEXA sodium phosphate from LDH nanohybrids.

Fig. 12**d** illustrates data fitted to the second-order model,

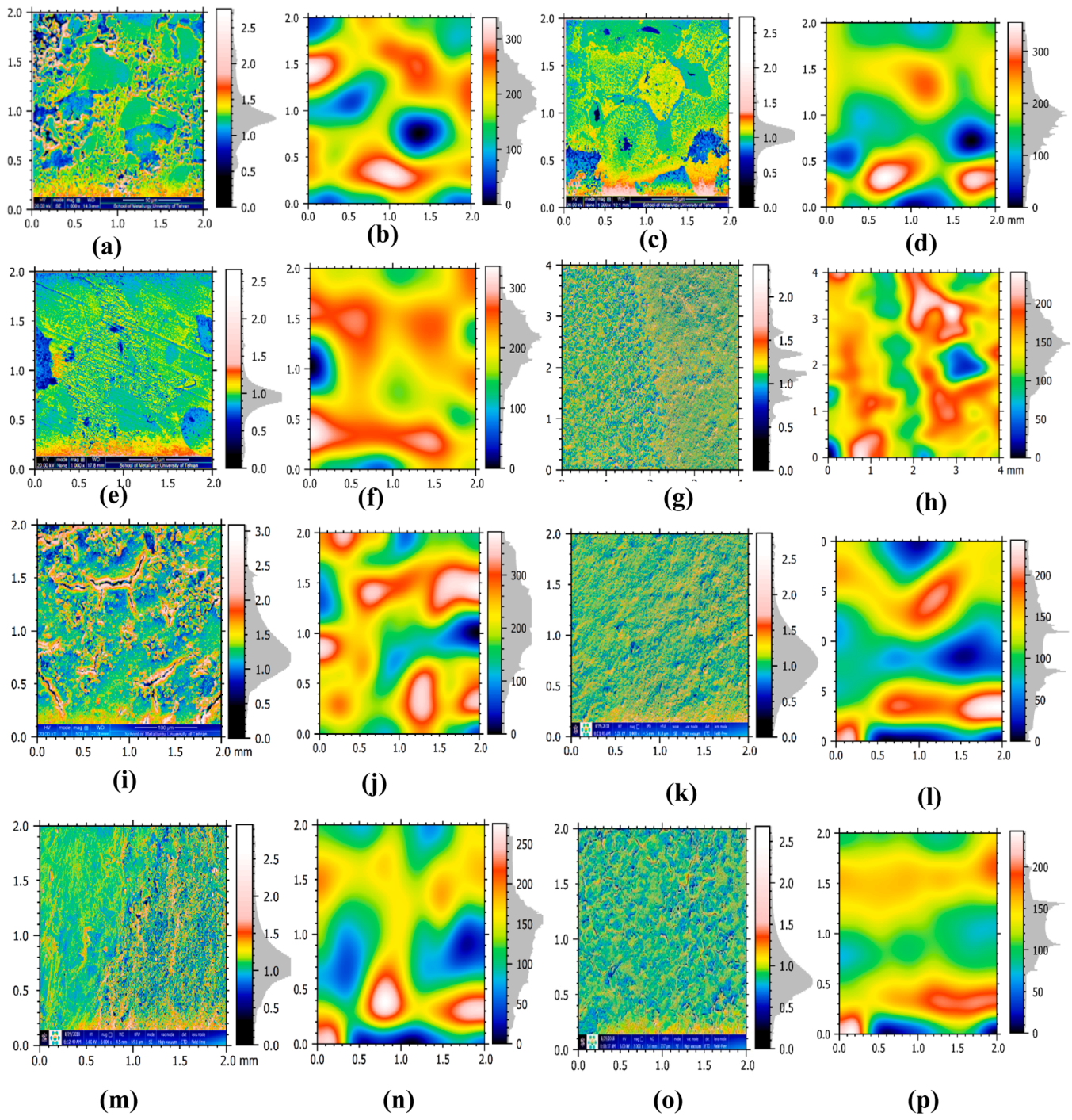

Fig. 9. Roughness and waviness contour plot for different samples: (a, b) CPS, (c, d) SPS, (e, f) ball-milled SPS, and coated samples at different voltages: (g, h) 30 V, (i, j) 40 V, (k, l) 50 V, (m, n) 60 V, (o, p) 80 V.

Table 3
Roughness and waviness values for different samples.

Samples	CPS	SPS	Ball milled SPS	30 V	40 V	50 V	60 V	80 V
Roughness (Sq) nm	0.3478	0.3088	0.2468	0.3222	0.4336	0.2997	0.3204	0.3708
Waviness (Sq) pm	63.04	53.04	47.46	36.2	69.88	33.36	49.62	48.88

demonstrating a linear relationship throughout the entire release period with the highest correlation coefficient ($R^2 > 0.99$) among the models discussed. Additionally, Fig. 12**e** shows data fitted to the parabolic diffusion model, which exhibits linearity only during initial release times, making it suitable for early drug release from LDHs with an appropriate R^2 value. Previous studies [36,64] have established that both dissolution and diffusion mechanisms play crucial roles in controlling the release kinetics of DEXA from hydrophilic LDHs

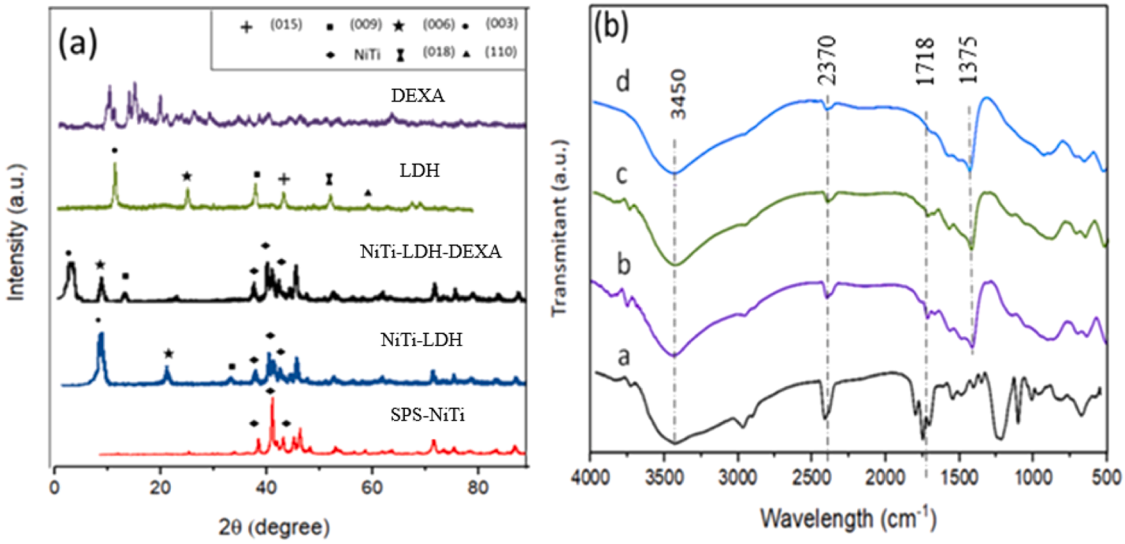

Fig. 10. (a) XRD patterns of different LDH base Nano-hybrids, (b) FT-IR patterns for LDH and DEXA with a weight ratio of a) 1:0, b) 1:1, c) 1:0.5, and d) 0:1.

Table 4
Basal distance and lattice parameters (LP) of main planes for three Types of LDHs.

Parameters (Å)	LDH	LDH-DEXA (1:0.5)	LDH-DEXA (1:1)
d_{003}	7.14538	9.5294	20.130
d_{006}	3.5832	4.4739	7.7251
d_{110}	1.4295	1.4299	1.5284
LP 'A'	2.859	2.8598	3.0568
LP 'C'	21.43614	28.5882	60.390

nanoparticles.

3.6. Corrosion results

Polarization curves were generated using the Tafel method for both uncoated and LDH-coated samples immersed in PBS electrolyte [70,71], as depicted in Fig. 13**a**. In corrosion testing, the current density derived from these curves serves to estimate the corrosion rate. After calculating the Tafel slopes, the corrosion current density (i_{corr}) and corrosion potential (E_{corr}) were determined to evaluate the corrosion properties. The methodology for calculating i_{corr} has been detailed in previous literature [72]. The Tafel extrapolation method was employed to ascertain the current densities from the polarization curves of different specimens. The results along with the corrosion potential for different samples are presented in Table 6. Results, including corrosion potentials for various samples, the corrosion potential of CPS uncoated specimens is more positive than that of SPS samples, likely due to the presence of oxide phases. Fig. 13**a** and Table 6 illustrate that the corrosion current density of the CPS samples is higher compared to the other two samples, possibly attributable to their higher porosity and increased exposure to the PBS solution. Coating the Nitinol surface with LDH, known for its Brucite-like properties, resulted in a more positive corrosion potential compared to the bare SPS specimen, accompanied by reduced current density, and enhanced corrosion resistance.

Furthermore, given that NiTi alloys are susceptible to corrosion in chloride-containing environments [73], the presence of LDHs can effectively improve corrosion resistance. According to the ion exchange theory, CO_3^{2-} and OH^- ions within LDHs interlayers can exchange with Cl^- ions under physiological conditions, thereby reducing the local Cl^- ion concentration near the surface [32]. Notably, CPS samples fail to conduct electrical current effectively to the surface due to the presence of an oxide layer, rendering them unsuitable for coating [46]. As anticipated, CPS samples exhibited a significantly higher corrosion rate compared to the other two types ($p < 0.01$). Additionally, LDH coating on SPS samples reduced the corrosion rate by approximately 31 %, as

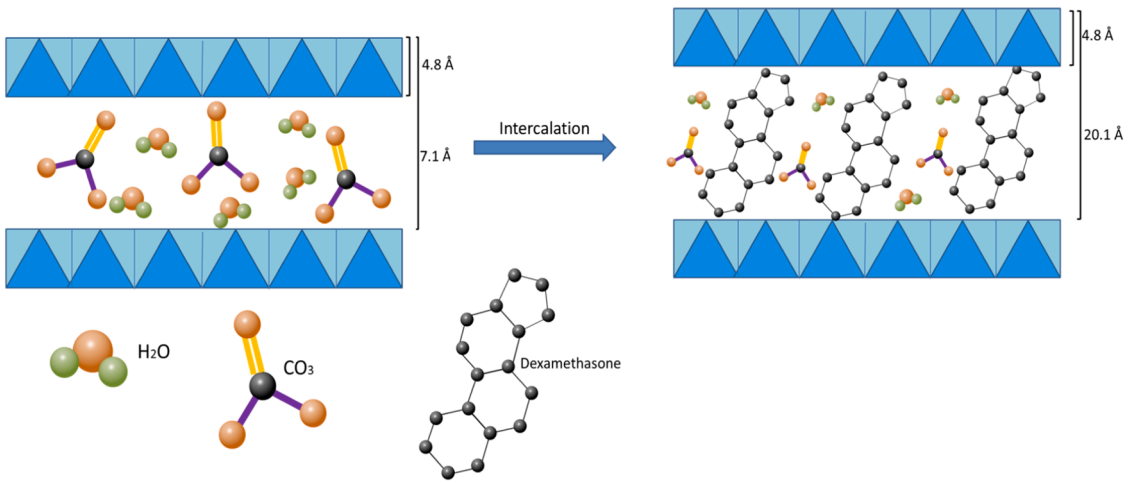

Fig. 11. Schematic illustration of the interaction of DEXA within the LDH galleries.

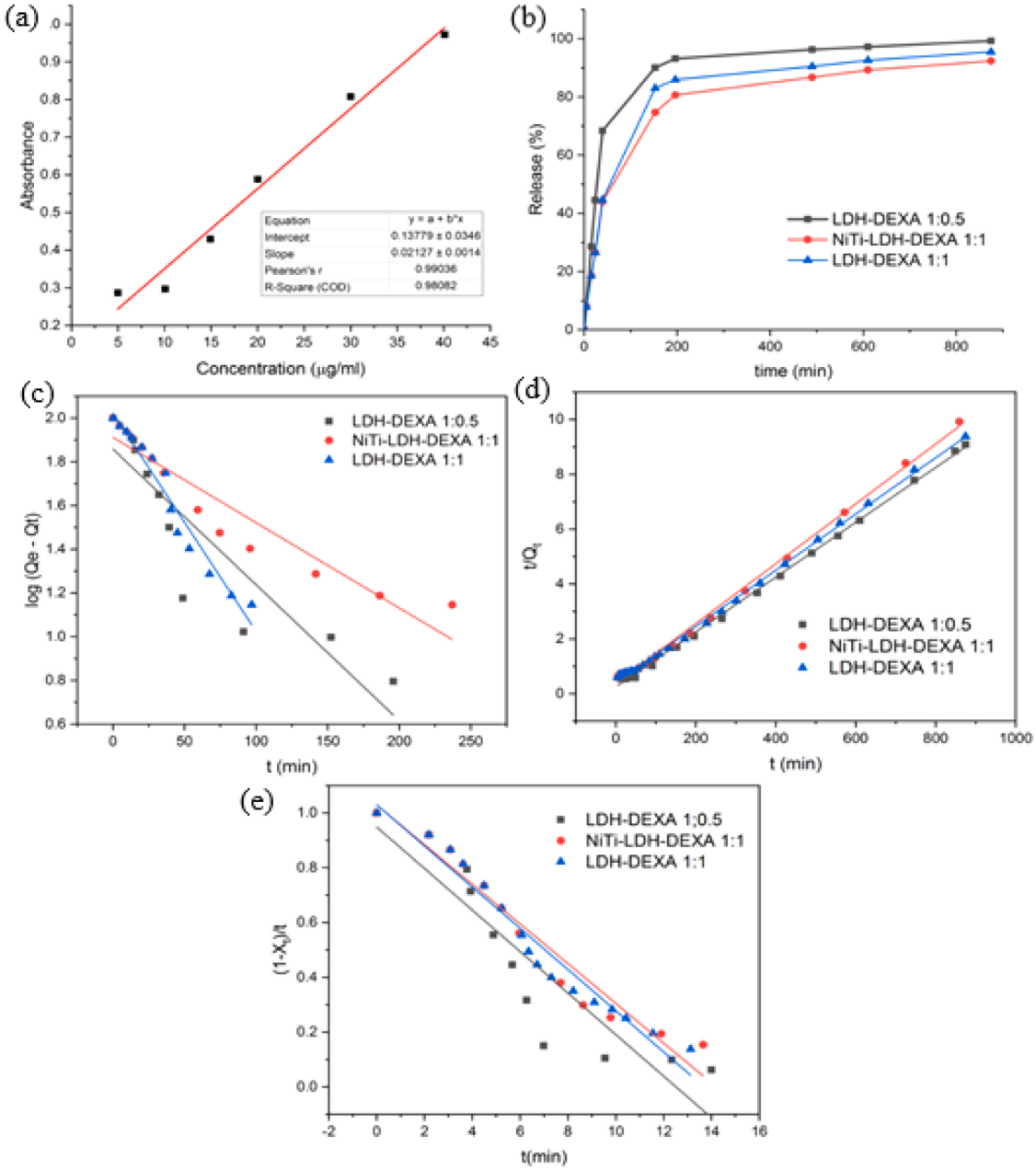

Fig. 12. **(a)** Calibration plot for DEXA at 242 nm, (b) Release profile of various samples over time for DEXA in PBS at PH=7.4 and 37°C, (c) First-order (d) second-order, and (e) parabolic kinetic profiles and fitted data for DEXA of various samples over time.

Table 5
Correlation factor (R^2) for fitted data to various kinetic models.

Sample	Pseudo-first-order	Pseudo-second-order	Parabolic diffusion
LDH-DEXA 1:1	0.9451	0.9994	0.9469
NiTi-LDH-DEXA 1:1	0.9353	0.9996	0.9569
LDH-DEXA 1:0.5	0.8112	0.9971	0.8419

shown in Fig. 13**b**.

3.7. Contact angles

The results of contact angle (CA) measurements, demonstrating the wettability of both bare and coated Nitinol specimens with water, are presented in Fig. 14. As expected, the bare Nitinol sample exhibited the highest CA compared to the coated samples with varying voltages. Fig. 14**c** clearly shows a decrease in CA values from 92.39° for the bare sample to 45.28° for the sample coated at 80 V. This indicates that coating the surface with LDH nanohybrids significantly enhanced both wettability and hydrophilicity.

Surface properties of materials play a crucial role in determining their interaction with the biological environment. Wettability in particular, provides insights into the adhesion and adsorptive behavior of a material. Furthermore, it can influence cell maturation and differentiation [74]. Hydrophobic materials are generally less conducive to cell attachment [75], whereas studies have suggested that hydrophilic surfaces promote osteoblast differentiation [76].

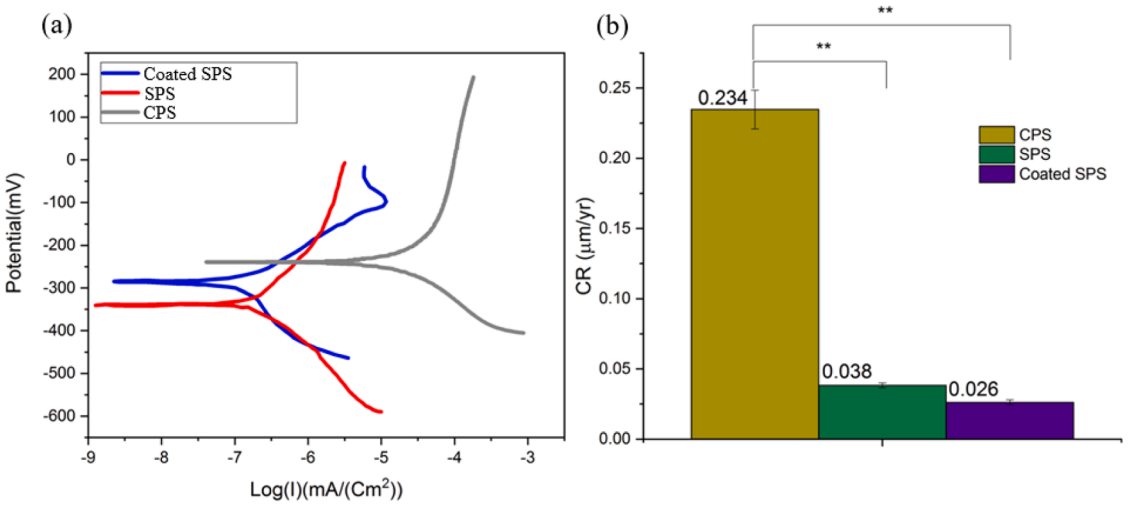

Fig. 13. (a) Polarization graphs and (b) corrosion rate values for uncoated and coated specimens.

Table 6
Polarization test results for uncoated and coated specimens.

Sample	E_{corr}(mV)	i_{corr}(mA/cm^2)	R_P (KΩ.cm^2)
CPS	−243.23	2.7E^{-3}	95.28
SPS	−341.35	4.4E^{-4}	580.3
Coated SPS	−287.27	3.009E^{-4}	864.47

3.8. Cell adhesion response

To assess the response of the coated Nitinol surface upon contact with the NIH 3T3 cells, FESEM images were captured and are presented in Fig. 15. The images reveal a satisfactory number of cells proliferating on the surface coated with LDH-nanohybrids after 24 h of culture (Fig. 15**a).** Additionally, Fig. 15**-b** demonstrates robust adhesion between the surface and fibroblast-like cells, characterized by well-spreading cells indicating favorable contact properties.

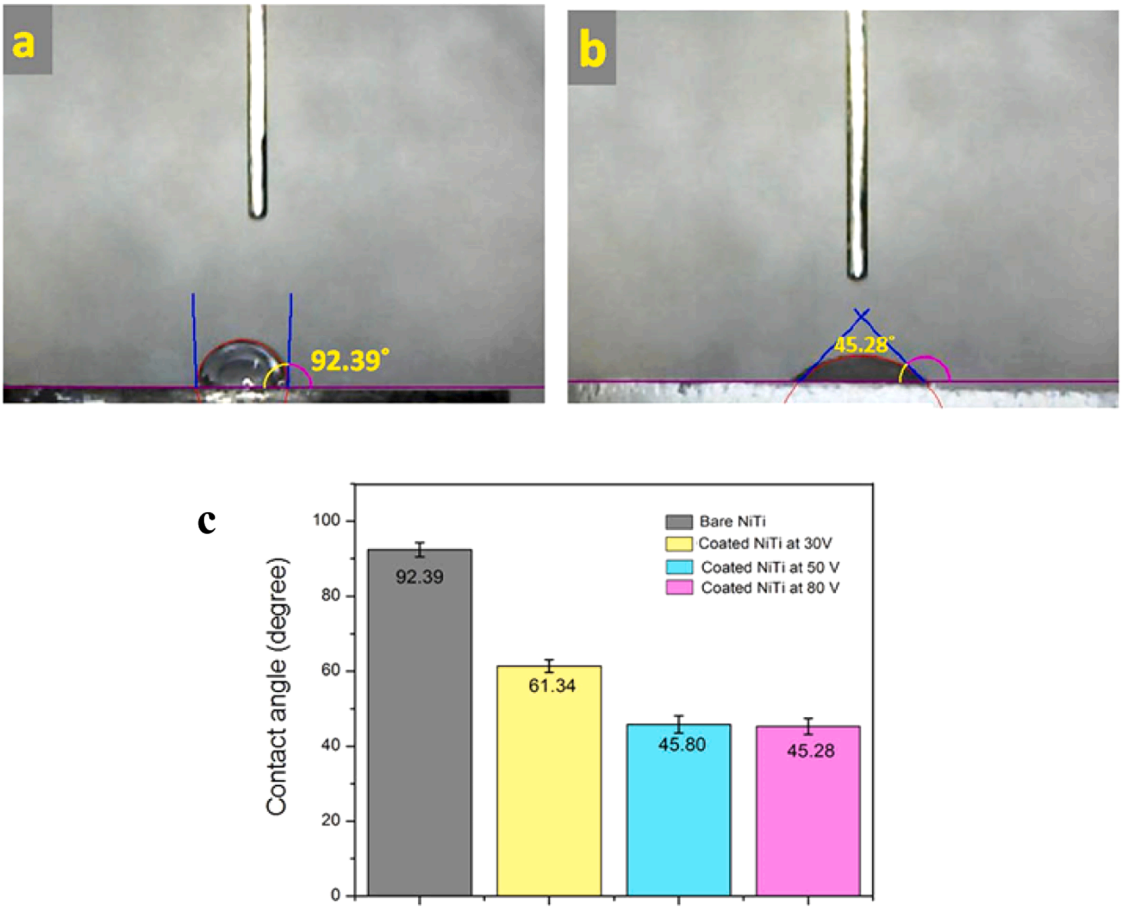

Fig. 14. Water droplet on the surface of (a) bare Nitinol and (b) coated at 80 V. (c) Contact angle measurements for different samples.

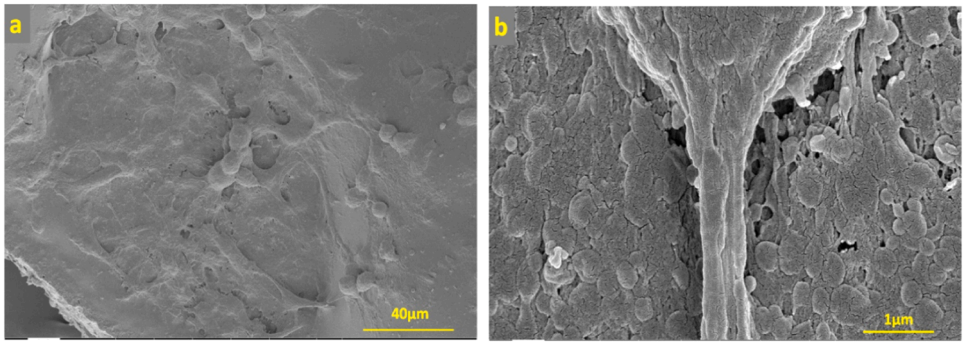

Fig. 15. FESEM images of NIH 3T3 cells on the coated surface of Nitinol showing (a) cell proliferation, and (b) cell adhesion.

4. Conclusion

This study successfully demonstrated the potential of enhancing Nitinol alloys with Al-Zn-LDH nanoparticles intercalated with dexamethasone sodium phosphate for improved biocompatibility, controlled drug release, and superior corrosion resistance. Using two consolidation methods, CPS and SPS, the results indicated that SPS samples, due to their denser and more homogeneous microstructures, were more suitable for subsequent coating and drug intercalation processes compared to CPS samples. Key findings highlighted that SPS samples achieved better microstructural homogeneity and reduced porosity, leading to enhanced mechanical properties and corrosion resistance. The successful intercalation of dexamethasone into the LDH layers increased the interlayer spacing from 7.14 Å to 20.130 Å, facilitating a more controlled drug release profile. Additionally, LDH-coated SPS samples exhibited significantly improved corrosion resistance in PBS environments, reducing the corrosion rate by approximately 31 % compared to uncoated samples.

These findings advance the field by providing a robust method for enhancing the performance of Nitinol implants through surface modification with LDH coatings and drug intercalation, offering dual benefits of controlled drug release and improved corrosion resistance, which are critical for biomedical applications, particularly in orthopedics and cardiovascular therapies. Future research should focus on long-term in vivo studies to assess the biocompatibility and therapeutic efficacy of LDH-coated Nitinol implants. Expanding the range of intercalated drugs, including anti-inflammatory, antibiotic, and growth factor molecules, could broaden the therapeutic applications of these coatings. Further optimization of EPD parameters can improve coating uniformity and adhesion, potentially enhancing the overall performance of the implants. These future directions will pave the way for developing next-generation Nitinol-based implants with multifunctional capabilities, thereby contributing significantly to the advancement of biomedical engineering.

CRediT authorship contribution statement

Mehrdad Khakbiz: Writing – review & editing, Writing – original draft, Visualization, Validation, Supervision, Software, Resources, Project administration, Methodology, Investigation, Conceptualization, supervision. **Saeed Sheibani:** Writing – review & editing, Investigation. **Seyedsajad Moazzeni:** Writing – review & editing, Investigation. **Milad Chagami:** Investigation, Data curation, Writing – original draft, Validation, Methodology. **Ki-Bum Lee:** Writing – review & editing. **Sara Shakibania:** Writing – review & editing. **Yannan Hou:** Writing – review & editing. **Elahe Amiri:** review & editing, Methodology.

Declaration of Competing Interest

The authors declare that they have no known competing financial interests or personal relationships that could have appeared to influence the work reported in this paper.

Acknowledgments

The authors would like to acknowledge technical support and valuable assistance of the Institutes for NanoBiomedical Research, Rutgers University. We are especially grateful to anonymous reviewers for their valuable and constructive comments.

Data availability

Data will be made available on request.

References

[1] L. Petrini, F. Migliavacca, Biomedical applications of shape memory alloys, J. Metall. 2011 (1) (2011) 501483.
[2] D. Kapoor, Nitinol for medical applications: a brief introduction to the properties and processing of nickel titanium shape memory alloys and their use in stents, Johns. Matthey Technol. Rev. 61 (1) (2017) 66–76.
[3] Kujala, S., *Biocompatibility and biomechanical aspects of Nitinol shape memory metal implants*. 2003: University of Oulu.
[4] P.S. Bagha, et al., Effect of high energy ball milling on the properties of biodegradable nanostructured Fe-35 wt% Mn alloy, J. Alloy. Compd. 768 (2018) 166–175.
[5] N. Sharma, K.K. Jangra, T. Raj, Fabrication of NiTi alloy: a review, Proc. Inst. Mech. Eng., Part L: J. Mater.: Des. Appl. 232 (3) (2018) 250–269.
[6] A. Bansiddhi, et al., Porous NiTi for bone implants: a review, Acta Biomater. 4 (4) (2008) 773–782.
[7] M.H. Elahinia, et al., Manufacturing and processing of NiTi implants: a review, Prog. Mater. Sci. 57 (5) (2012) 911–946.
[8] M. Bram, et al., Powder metallurgical fabrication processes for NiTi shape memory alloy parts, Mater. Sci. Eng.: A 337 (1-2) (2002) 254–263.
[9] S.S.S. POMO, S.Z.I. PLAZMO, Powder-metallurgy preparation of NiTi shape-memory alloy using mechanical alloying and spark-plasma sintering, POWDER-Metall. 141 (2017) 144.
[10] N. Zhang, et al., TiNi shape memory alloys prepared by normal sintering, Mater. Sci. Eng.: A 150 (2) (1992) 263–270.
[11] J. Butler, et al., Production of nitinol wire from elemental nickel and titanium powders through spark plasma sintering and extrusion, J. Mater. Eng. Perform. 20 (2011) 757–761.
[12] J. Weng, et al., Formation and characteristics of the apatite layer on plasma-sprayed hydroxyapatite coatings in simulated body fluid, Biomaterials 18 (15) (1997) 1027–1035.
[13] P. Shi, F. Geng, F. Cheng, Preparation of titania–hydroxyapatite coating on NiTi via a low-temperature route, Mater. Lett. 60 (16) (2006) 1996–1999.
[14] B. Aksakal, C. Hanyaloglu, Bioceramic dip-coating on Ti–6Al–4V and 316L SS implant Materials. J. Mater. Sci.: Mater. Med. 19 (2008) 2097–2104.
[15] Anders, A., *Handbook of plasma immersion ion implantation and deposition*. Vol. 8. 2000: Wiley New York.
[16] J. Wang, et al., Biomimetic and electrolytic calcium phosphate coatings on titanium alloy: physicochemical characteristics and cell attachment, Biomaterials 25 (4) (2004) 583–592.
[17] A. Boccaccini, et al., Electrophoretic deposition of biomaterials, J. R. Soc. Interface 7 (suppl_5) (2010) S581–S613.
[18] S. Manara, et al., Electrochemically-assisted deposition of biomimetic hydroxyapatite–collagen coatings on titanium plate, Inorg. Chim. Acta 361 (6) (2008) 1634–1645.
[19] I. Corni, M.P. Ryan, A.R. Boccaccini, Electrophoretic deposition: From traditional ceramics to nanotechnology, J. Eur. Ceram. Soc. 28 (7) (2008) 1353–1367.

[20] W. Chen, L. Feng, B. Qu, Preparation of nanocomposites by exfoliation of ZnAl layered double hydroxides in nonpolar LLDPE solution, Chem. Mater. 16 (3) (2004) 368–370.
[21] L. Aimoz, et al., Order of cation and anion in iodide-containing hydrotalcite-like minerals, J. Phys. Chem. C. 116 (2012) 5460–5475.
[22] J.-H. Yang, et al., New inorganic-based drug delivery system of indole-3-acetic acid-layered metal hydroxide nanohybrids with controlled release rate, Chem. Mater. 19 (10) (2007) 2679–2685.
[23] A. Radha, P.V. Kamath, C. Shivakumara, Mechanism of the anion exchange reactions of the layered double hydroxides (LDHs) of Ca and Mg with Al, Solid State Sci. 7 (10) (2005) 1180–1187.
[24] J.-H. Choy, et al., *Cellular uptake behavior of [γ-32P] labeled ATP–LDH nanohybridsElectronic supplementary information (ESI) available: histogram for Mg solubility of Mg2Al–LDH as a function of pH; FITC–LDH exchange rate according to NaCl concentration (FITC= fluorescein 5-isothiocyanate); cytotoxicity test of Mg2Al–NO3−–LDH. See* http://www. *rsc. org/suppdata/jm/b0/b008680k*, J. Mater. Chem. 11 (6) (2001) 1671–1674.
[25] J.-H. Choy, et al., Intercalative nanohybrids of nucleoside monophosphates and DNA in layered metal hydroxide, J. Am. Chem. Soc. 121 (6) (1999) 1399–1400.
[26] J.H. Choy, et al., Inorganic layered double hydroxides as nonviral vectors, Angew. Chem. Int. Ed. 39 (22) (2000) 4041–4045.
[27] A. Yasutake, et al., Synthesis of biopolymer intercalated inorganic-layered materials: Intercalation of collagen peptide and soybean peptide into Zn–Al layered double hydroxide and layered zinc hydroxide, J. Phys. Chem. Solids 69 (5-6) (2008) 1542–1546.
[28] B. Li, et al., Inorganic layered double hydroxides as a drug delivery system—intercalation and in vitro release of fenbufen. Appl. clay Sci. 27 (3-4) (2004) 199–207.
[29] A. Alcantara, et al., Bionanocomposites based on alginate–zein/layered double hydroxide materials as drug delivery systems, J. Mater. Chem. 20 (42) (2010) 9495–9504.
[30] Buchheit Jr, R.G. and G.E. Stoner, *Method for increasing the corrosion resistance of aluminum and aluminum alloys*. 1997, Google Patents.
[31] J.-Y. Uan, J.-K. Lin, Y.-S. Tung, Direct growth of oriented Mg–Al layered double hydroxide film on Mg alloy in aqueous HCO 3−/CO 3 2− solution, J. Mater. Chem. 20 (4) (2010) 761–766.
[32] F. Peng, et al., Enhanced corrosion resistance and biocompatibility of magnesium alloy by Mg–Al-layered double hydroxide. ACS Appl. Mater. Interfaces 8 (51) (2016) 35033–35044.
[33] N. Safaie, et al., Synthesizing of nanostructured Fe-Mn alloys by mechanical alloying process, Procedia Mater. Sci. 11 (2015) 381–385.
[34] F. Zhang, et al., Corrosion resistance of superhydrophobic Mg–Al layered double hydroxide coatings on aluminum alloys, Acta Metall. Sin. (Engl. Lett.) 28 (2015) 1373–1381.
[35] T. Ishizaki, et al., Corrosion resistance of Mg–Al layered double hydroxide container-containing magnesium hydroxide films formed directly on magnesium alloy by chemical-free steam coating, J. Mater. Chem. A 1 (31) (2013) 8968–8977.
[36] L. Guo, et al., Layered double hydroxide coatings on magnesium alloys: a review, J. Mater. Sci. Technol. 34 (9) (2018) 1455–1466.
[37] J. Wang, et al., Hydrotalcite conversion coating on Mg alloy and its corrosion resistance, J. Alloy. Compd. 494 (1-2) (2010) 271–274.
[38] J.-H. Syu, et al., Optically transparent Li–Al–CO3 layered double hydroxide thin films on an AZ31 Mg alloy formed by electrochemical deposition and their corrosion resistance in a dilute chloride environment, Corros. Sci. 68 (2013) 238–248.
[39] S. He, et al., Preparation of oriented layered double hydroxide film using electrophoretic deposition and its application in water treatment, Ind. Eng. Chem. Res. 50 (5) (2011) 2800–2806.
[40] A. Matsuda, et al., Characterization and film properties of electrophoretically deposited nanosheets of anionic titanate and cationic MgAl-layered double hydroxide, J. Phys. Chem. B 117 (6) (2013) 1724–1730.
[41] F.S. Vajedi, H. Dehghani, A high-sensitive electrochemical DNA biosensor based on a novel ZnAl/layered double hydroxide modified cobalt ferrite-graphene oxide nanocomposite electrophoretically deposited onto FTO substrate for electroanalytical studies of etoposide, Talanta 208 (2020) 120444.
[42] X. Li, et al., Ni/Al layered double hydroxide nanosheet film grown directly on Ti substrate and its application for a nonenzymatic glucose sensor, Sens. Actuators B: Chem. 147 (1) (2010) 241–247.
[43] J.H. Lee, D.-Y. Jung, Highly oriented nanoplates of layered double hydroxides as an ultra slow release system, Chem. Commun. 48 (45) (2012) 5641–5643.
[44] Y. Wang, et al., Facile fabrication of a nanosphere film from layered double hydroxide nanosheets using an electrophoretic deposition method, Electrochem. Commun. 10 (9) (2008) 1264–1267.
[45] M. Bartmanski, et al., Effects of solution composition and electrophoretic deposition voltage on various properties of nanohydroxyapatite coatings on the Ti13Zr13Nb alloy, Ceram. Int. 44 (16) (2018) 19236–19246.
[46] H. Maleki-Ghaleh, et al., Effect of hydroxyapatite coating fabricated by electrophoretic deposition method on corrosion behavior and nickel release of NiTi shape memory alloy, Mater. Corros. 65 (7) (2014) 725–732.
[47] A. Kamyar, et al., Synthesis of a novel dexamethasone intercalated layered double hydroxide nanohybrids and their deposition on anodized titanium nanotubes for drug delivery purposes, J. Solid State Chem. 271 (2019) 144–153.
[48] K.V. Kumar, I.A. Khaddour, V.K. Gupta, A pseudo second-order kinetic expression for dissolution kinetic profiles of solids in solutions, Ind. Eng. Chem. Res. 49 (16) (2010) 7257–7262.
[49] M.T. Banizi, et al., Functionalized high entropy alloys with ZIF-8 and LDH nanolayers for next-generation drug eluting medical implants, J. Alloy. Compd. 997 (2024) 174883.
[50] Lagergren, S., *About the theory of so-called adsorption of soluble substances*. 1898.
[51] Liu, X. *Data Reconciliation of Release Mechanism Research of LDH-Based Drug. in Advances in Swarm Intelligence: 4th International Conference, ICSI 2013, Harbin, China, June 12-15, 2013, Proceedings, Part II 4. 2013*. Springer.
[52] C. Shearwood, et al., Spark plasma sintering of TiNi nano-powder, Scr. Mater. 52 (6) (2005) 455–460.
[53] P. Salvetr, et al., Influence of heat treatment on microstructure and properties of NiTi46 alloy consolidated by spark plasma sintering, Materials 12 (24) (2019) 4075.
[54] S. Sadrnezhaad, A. Selahi, Effect of mechanical alloying and sintering on Ni–Ti powders, Mater. Manuf. Process. 19 (3) (2004) 475–486.
[55] A.R. Boccaccini, et al., Electrophoretic deposition of carbon nanotubes, Carbon 44 (15) (2006) 3149–3160.
[56] L. Besra, M. Liu, A review on fundamentals and applications of electrophoretic deposition (EPD), Prog. Mater. Sci. 52 (1) (2007) 1–61.
[57] P. Zhao, et al., Electrophoretic deposition of carbon nanotubes on semi-conducting and non-conducting substrates, Electrochem. Commun. 108 (2019) 106558.
[58] L. Zhang, et al., Superelastic behaviors of biomedical porous NiTi alloy with high porosity and large pore size prepared by spark plasma sintering, J. Alloy. Compd. 644 (2015) 513–522.
[59] B. Bertheville, M. Neudenberger, J.-E. Bidaux, Powder sintering and shape-memory behaviour of NiTi compacts synthesized from Ni and TiH2, Mater. Sci. Eng.: A 384 (1-2) (2004) 143–150.
[60] M. Etminanfar, J. Khalil-Allafi, On the electrodeposition of Ca-P coatings on nitinol alloy: a comparison between different surface modification methods, J. Mater. Eng. Perform. 25 (2016) 466–473.
[61] G. Zhao, et al., High surface energy enhances cell response to titanium substrate microstructure, J. Biomed. Mater. Res. Part A: Off. J. Soc. Biomater., Jpn. Soc. Biomater., Aust. Soc. Biomater. Korean Soc. Biomater. 74 (1) (2005) 49–58.
[62] Z. Rezvani, M. Sarkarat, Synthesis and characterization of magnetic composites: intercalation of naproxen into Mg-Al layered double hydroxides coated on Fe3O4, Z. F. üR. Anorg. und Allg. Chem. 638 (5) (2012) 874–880.
[63] Z. Rezvani, M. Shahbaei, Bionanocomposites based on alginate and chitosan/layered double hydroxide with ciprofloxacin drug: investigation of structure and controlled release properties, Polym. Compos. 36 (10) (2015) 1819–1825.
[64] P. Sahoo, H. Panda, D. Bahadur, Studies on the stability and kinetics of drug release of dexamethasone phosphate intercalated layered double hydroxides nanohybrids, Mater. Chem. Phys. 142 (1) (2013) 106–112.
[65] F. Barahuie, et al., Drug delivery system for an anticancer agent, chlorogenate-Zn/Al-layered double hydroxide nanohybrid synthesised using direct co-precipitation and ion exchange methods, J. Solid State Chem. 217 (2014) 31–41.
[66] C. Gomes, et al., Use of ZnAl-layered double hydroxide (LDH) to extend the service life of reinforced concrete, Materials 13 (7) (2020) 1769.
[67] F.Z. Mahjoubi, et al., Zn–Al layered double hydroxides intercalated with carbonate, nitrate, chloride and sulphate ions: synthesis, characterisation and dye removal properties, J. Taibah Univ. Sci. 11 (1) (2017) 90–100.
[68] Y. Cao, et al., Insight into the fabrication of ZnAl layered double hydroxides intercalated with organic anions and their corrosion protection of steel reinforced concrete, J. Electrochem. Soc. 166 (16) (2019) C617.
[69] W.-R. Wang, et al., Dexamethasone sodium phosphate intercalated layered double hydroxides and their therapeutic efficacy in a murine asthma model, RSC Adv. 5 (30) (2015) 23826–23834.
[70] Y. Sun, et al., Electrochemical stability, corrosion behavior, and biological properties of Ni–Ti–O nanoporous layers anodically on NiTi alloy. Corros. Sci. 179 (2021) 109104.
[71] Y. Zhao, et al., Low-temperature alkali corrosion induced growth of nanosheet layers on NiTi alloy and their corrosion behavior and biological responses, Corros. Sci. 190 (2021) 109654.
[72] G. Engelhard, L. McMillion, D. Macdonald, A mathematical model for crevice corrosion under porous deposits, J. Nucl. Mater. 379 (1-3) (2008) 48–53.
[73] F. Xie, et al., Effects of hydroxyapatite addition on corrosion behavior and in-vitro bioactivity of Ti-10Mo matrix biocomposite, Mater. Today Commun. 31 (2022) 103787.
[74] X. Li, et al., Influence of fluoride and chloride on corrosion behavior of NiTi orthodontic wires, Acta Biomater. 3 (5) (2007) 807–815.
[75] M. Pacha-Olivenza, et al., Effect of UV irradiation on the surface Gibbs energy of Ti6Al4V and thermally oxidized Ti6Al4V, J. Colloid Interface Sci. 320 (1) (2008) 117–124.
[76] Y. Wang, et al., Modification of bone graft by blending with lecithin to improve hydrophilicity and biocompatibility, Biomed. Mater. 3 (1) (2008) 015012.